nature portfolio

https://doi.org/10.1038/s41593-021-00849-x

Supplementary information

Wireless multilateral devices for optogenetic studies of individual and social behaviors

In the format provided by the authors and unedited

Supplementary Figure 1 – Simple head-mounted devices

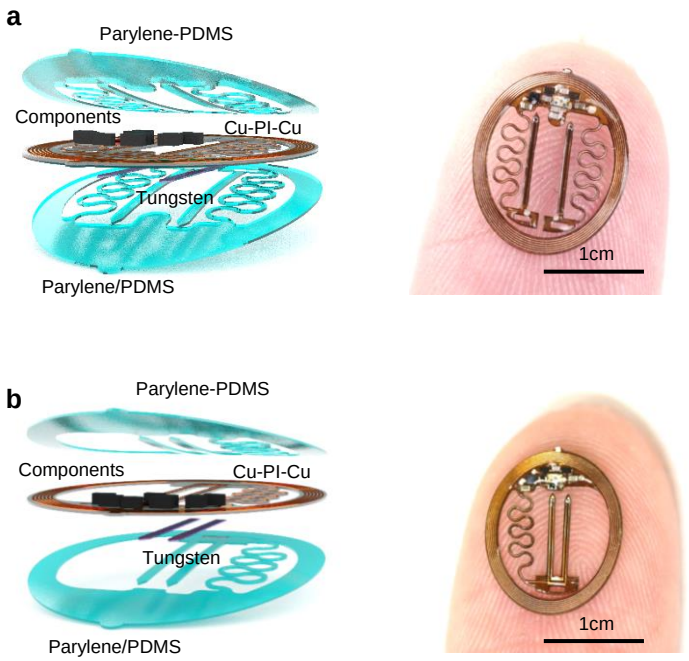

Figure S1. Simple head-mounted devices. a, Schematic illustrations (left) and photograph (right) of a head mounted device with independent bilateral probes that connect to stretchable serpentines. This device provides voltage regulation. **b,** Schematic illustrations (left) and photograph (right) of a head mounted device with dependent bilateral probes that connect to stretchable serpentines. This device also provides voltage regulation.

Supplementary Figure 2 – Implantation process for the simplified head-mounted device for mice

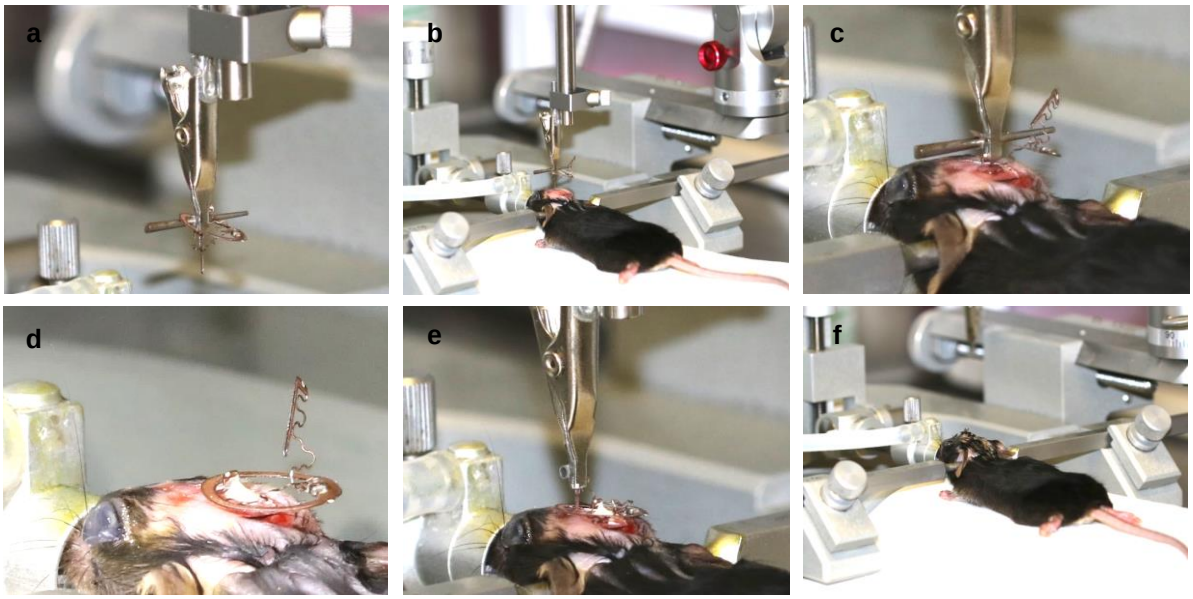

Figure S2. Implantation process for the simplified head-mounted device for mice. a, Clamp the first probe with a surgical clip that mounts on a stereotaxic apparatus. **b,** Confirm the implantation coordinates. **c,** Drill holes on coordinate locations and inject the first probe into the brain. **d,** Use dental cement to fix the position of the injected probe. **e,** Inject the second probe following the same steps shown in (**c**)-(**d**). **f,** Suture the incision on the skin and proceed with post-surgical procedures and monitoring according to institutional guidelines.

Supplementary Figure 3 – Implantation process for the head-mounted device with dynamically programmable channel operation system for mice

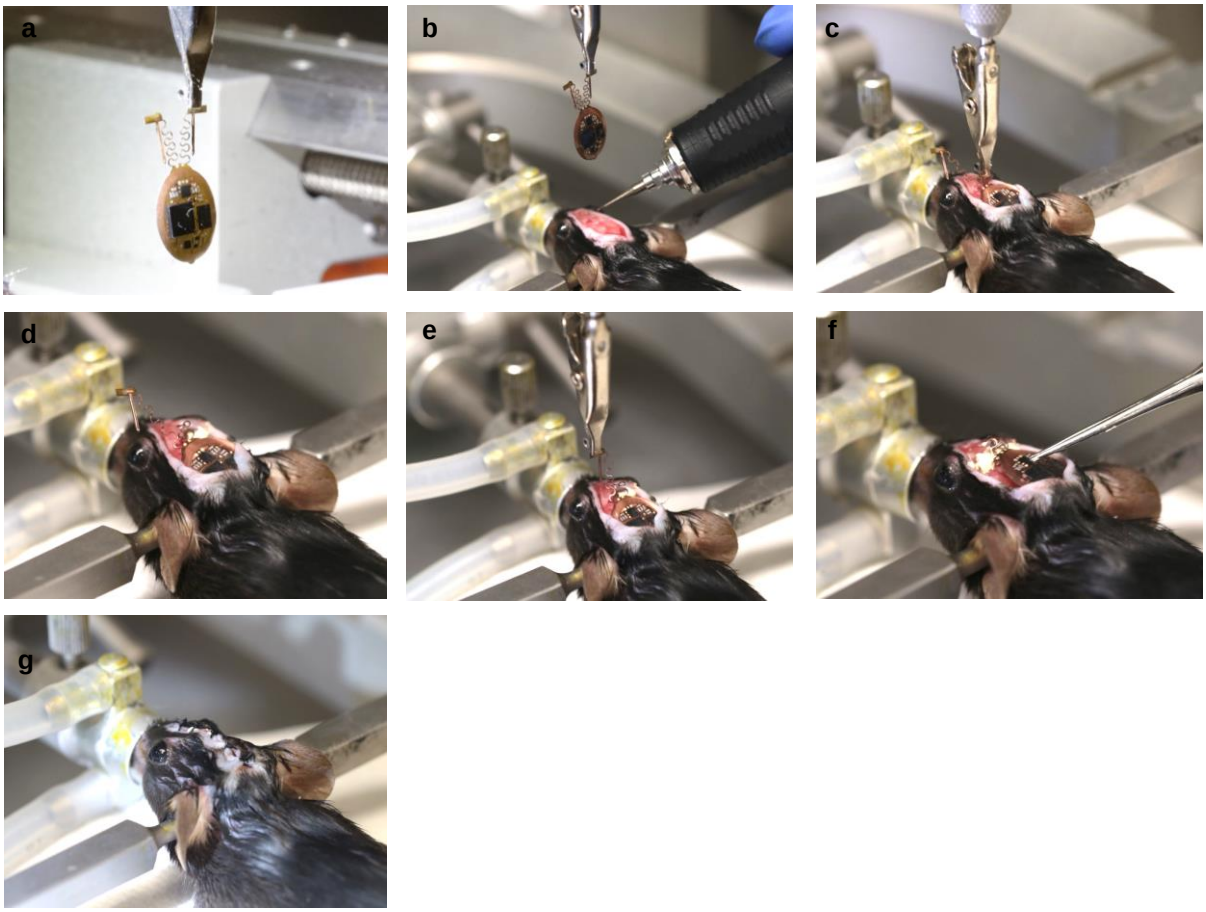

Figure S3. Implantation process for the head-mounted device with dynamically programmable channel operation system for mice. a, Clamp the first probe with a surgical clip that mounts on a stereotaxic arm. **b** Confirm the implantation coordinates and drill injection holes in the skull. **c,** Inject the first probe into the brain. **d,** Use cyanoacrylate to fix the position of the injected probe. **e,** Inject the second probe. **f,** Use cyanoacrylate to fix the position of the second injected probe. **g,** Suture the incision on the skin and proceed with post-surgical procedures and monitoring according to institutional guidelines.

Supplement Figure 4 – Implantation process for the back-mounted device for mice

Figure S4. Implantation process for the back-mounted device for mice. a, Cut the skin on the head and expose the skull. **b**, Make an incision on the back. **c,** Open a pocket through scalp incision towards back incision. **d,** Confirm the implantation coordinates and drill injection holes in the skull. **e,** Implant the device subdermally through the scalp incision. **f,** Pull the device towards back incision. **g,** Inject the first probe. **h,** Inject the second probe. **i,** Use dental cement to fix positions of injected probes. **j,** Suture the incision on the skin and proceed with post-surgical procedures and monitoring according to institutional guidelines.

Supplement Figure 5 – Implantation process for the back-mounted device for rats

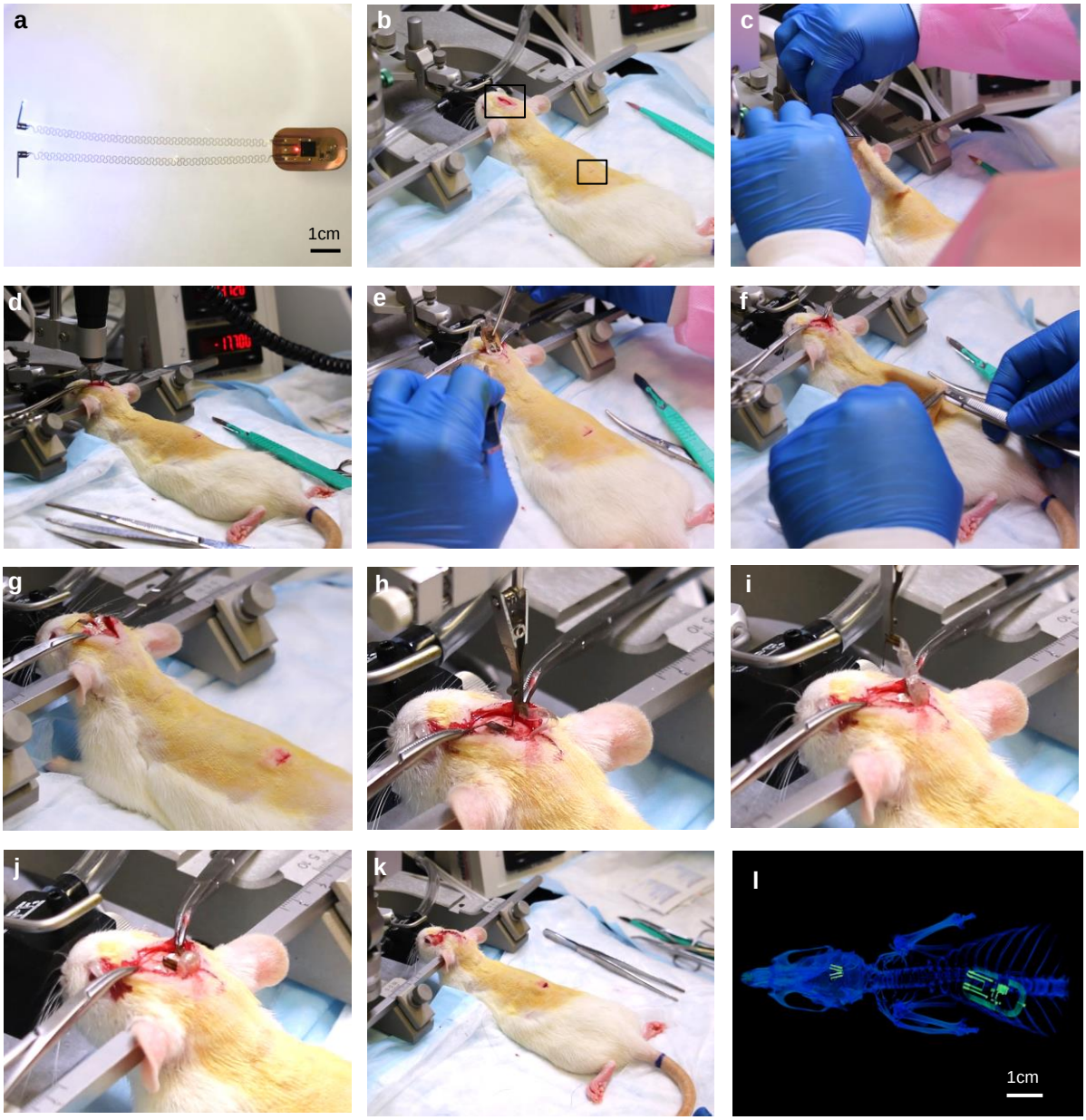

Figure S5. Implantation process for the back-mounted device for rats. a, Photograph of back subdermally mounted power regulated bilateral device for rats. **b,** Cut incisions on the head and the back. **c,** Open a pocket through head incision towards back incision. **d,** Confirm the implantation coordinates and drill injection holes in the skull. **e,** Implant device subdermally through head incision. **f,** Slide device towards back incision. **g,** Adjust the device position. **h,** Inject the first probe and secure with cyanoacrylate. **i,** Inject the second probe and secure with cyanoacrylate. **j,** Use dental cement to fix positions of injected probes. **k,** Suture the incision on the skin and proceed with post-surgical procedures and monitoring according to institutional guidelines. **l,** CT image of implanted back subdermal device in rat.

Supplementary Figure 6 – Fabrication scheme for the receiver coil and the electronic system of the back-mounted device

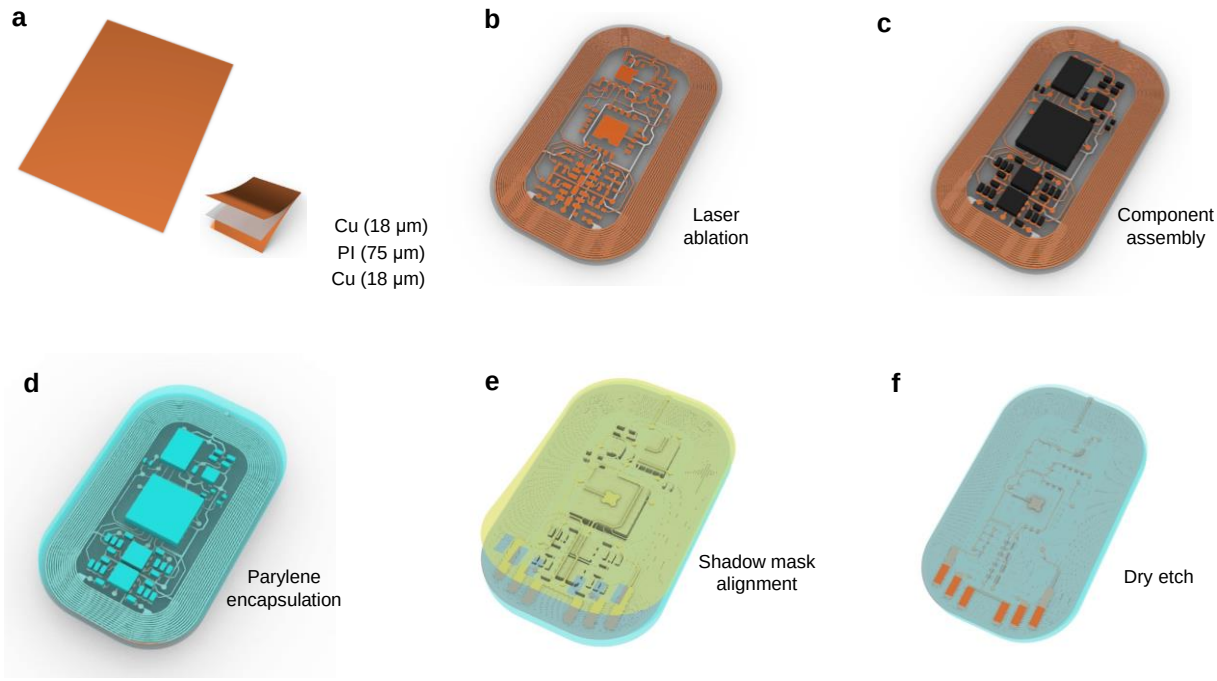

Figure S6. Fabrication scheme for the receiver coil and the electronic system for the back-mounted device. a, Prepare Pyralux Cu (18 μm)/PI (75 μm)/Cu (18 μm) sheet. **b,** Use laser to cut receiver coil and circuit footprint. **c,** Assemble electronic components. **d,** Coat parylene (14 μm). **e,** Attach PI (75 μm) shadow mask with contact pads exposed. **f,** Etch exposed parylene on contact pads for connection.

Supplementary Figure 7 – Fabrication scheme for the probes of the back-mounted device

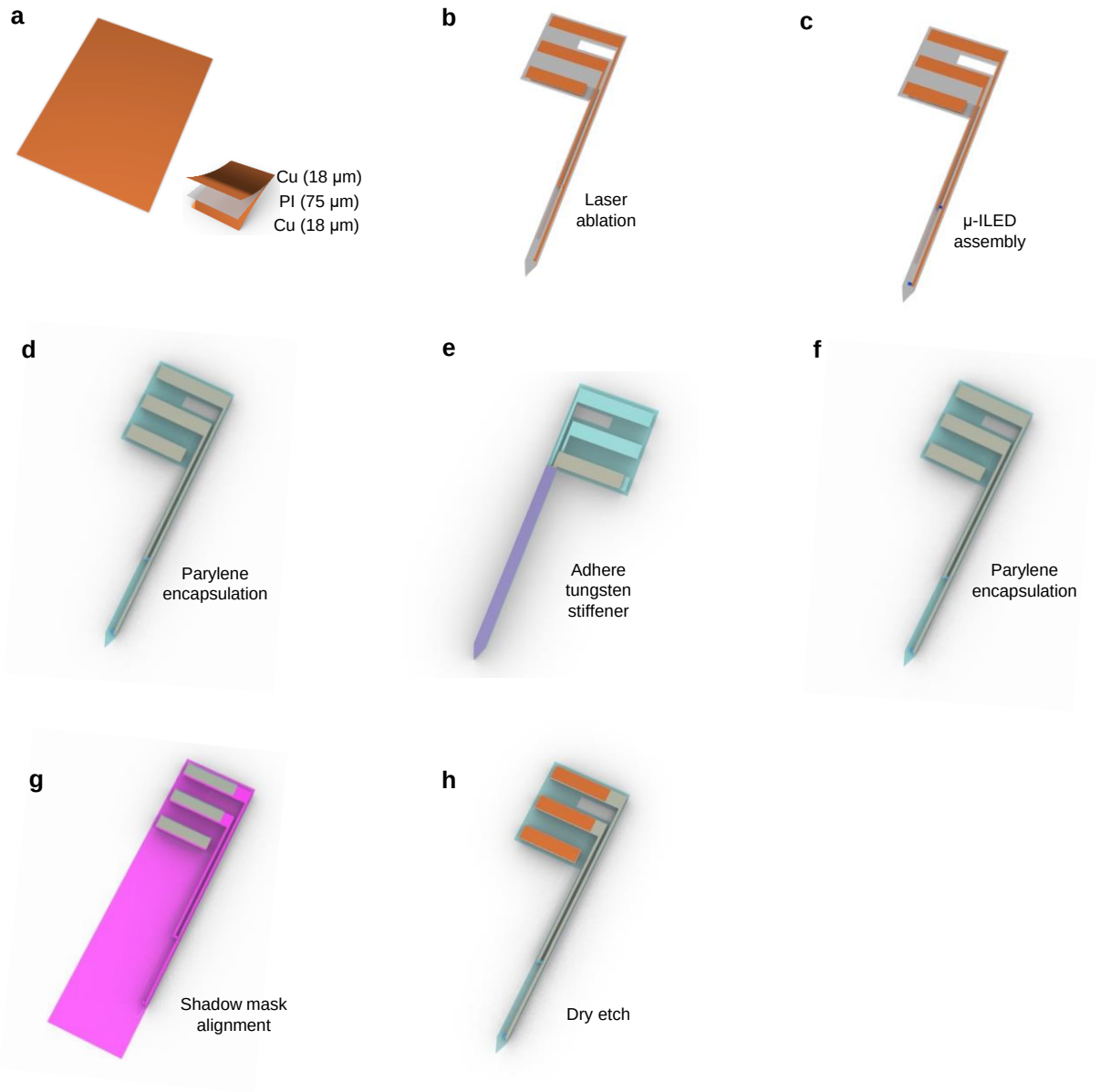

Figure S7. Fabrication scheme for the probes of the back-mounted device. a, Prepare Pyralux Cu (18 μm)/PI (75 μm)/ Cu (18 μm) sheet. **b,** Use laser to cut probe geometry. **c,** Assemble μ-ILEDs. **d,** Coat parylene (14 μm). **e,** Adhere tungsten stiffener with thin layer of epoxy. **f,** Coat parylene (14 μm). **g,** Attach PI (75 μm) shadow mask with contact pads exposed. **h,** Etch exposed parylene on contact pads for connection.

Supplementary Figure 8 – Fabrication scheme for the soft serpentine traces of the back-mounted device

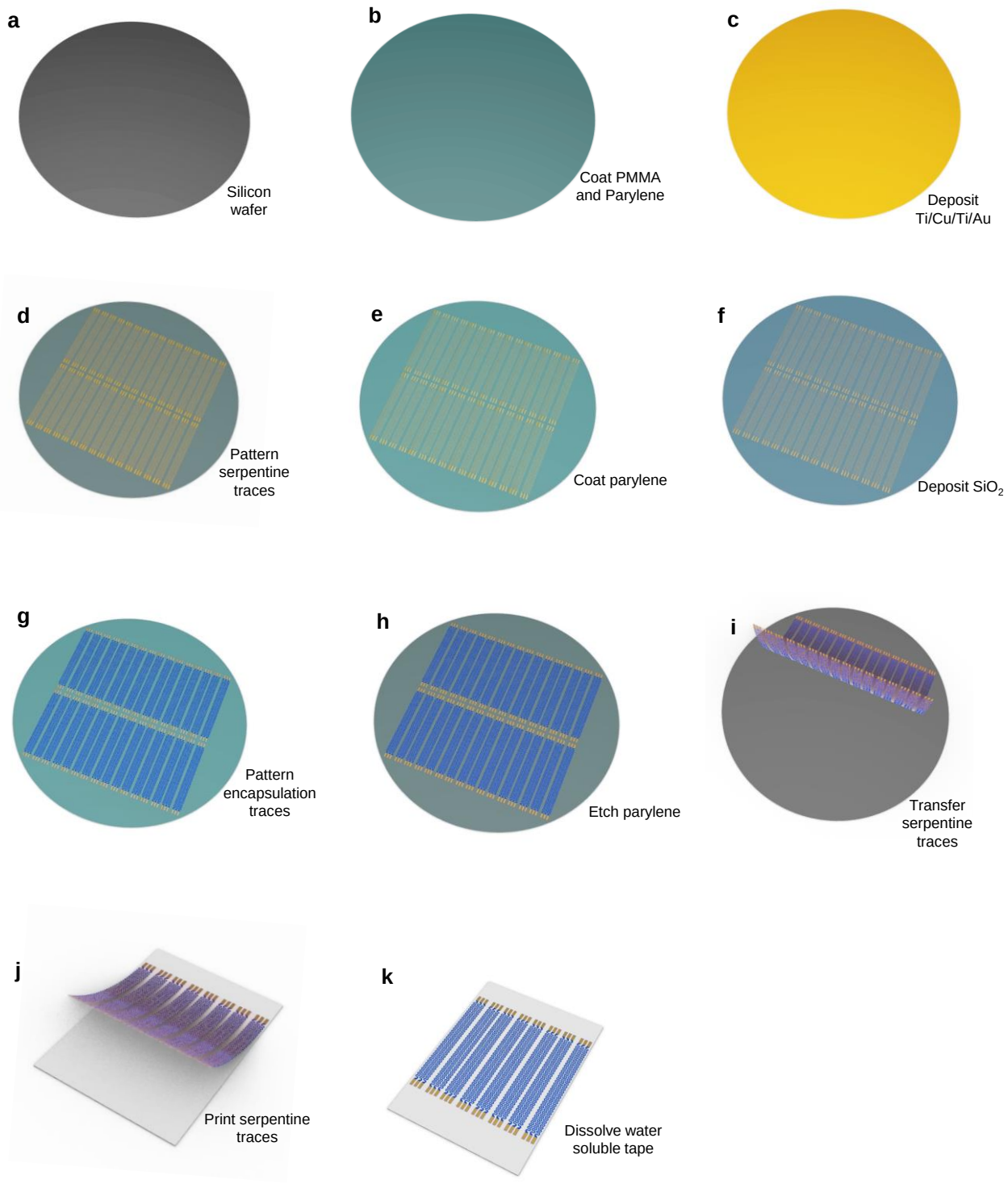

Figure S8. Fabrication scheme for the soft serpentine traces of the back-mounted device. a, Prepare silicon wafer. **b,** Coat PMMA (500 nm) and parylene (5 µm). **c,** Deposit Ti (20 nm)/Cu (300 nm)/Ti (20 nm)/Au (50 nm) **d,** Lithographically pattern metal serpentine traces. **e,** Coat parylene (5 µm). **f,** Deposit SiO_2 (60 nm). **g,** Pattern serpentine traces that encapsulate the metal traces with connection pads exposed on SiO_2 through lithography and RIE etching. **h,** Etch parylene through RIE. **i,** Dissolve PMMA and transfer serpentine traces with water soluble tape. **j,** Deposit 30 nm SiO_2 on water soluble tape and print serpentine traces on plasma treated Ecoflex. **k,** Dissolve water soluble tape in DI water.

Supplementary Figure 9: Pulse voltage modulation

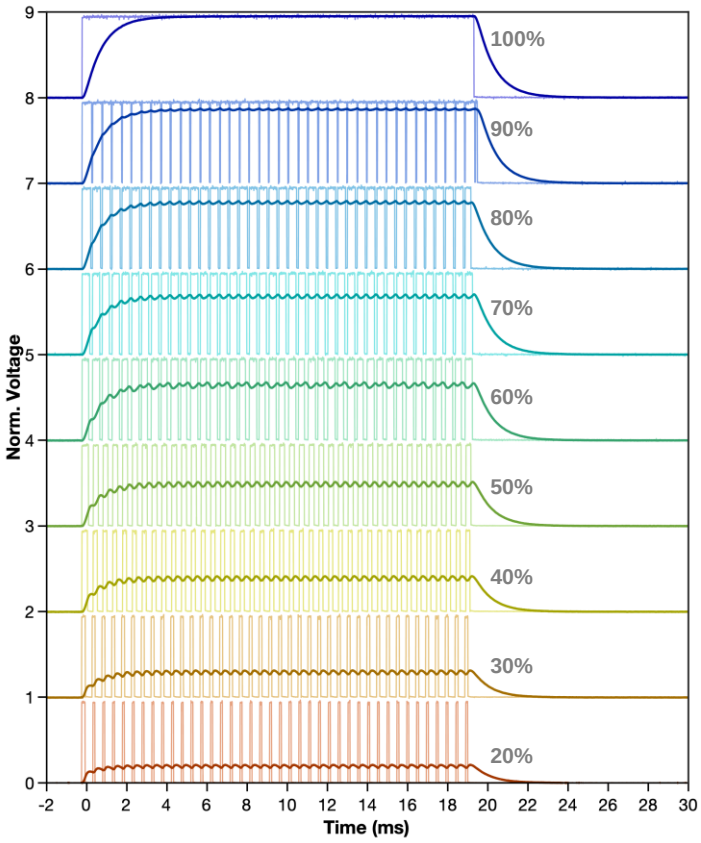

Figure S9. Pulse voltage modulation. Signal traces that illustrate the evolution of the signal as it passes the second order passive low-pass filter. The microcontrollers output a low frequency signal (10 Hz in this example at 20% duty cycle) that amplitude modulates a high frequency (2 kHz) carrier. The filtered pulse voltage depends on the duty cycle of the carrier as shown in the figure for duty cycles from 20 to 100%. In the absence of the second order low pass filter this mode of operation provides programable burst mode of operation.

Supplementary Figure 10: Demonstration of pulse duration limits

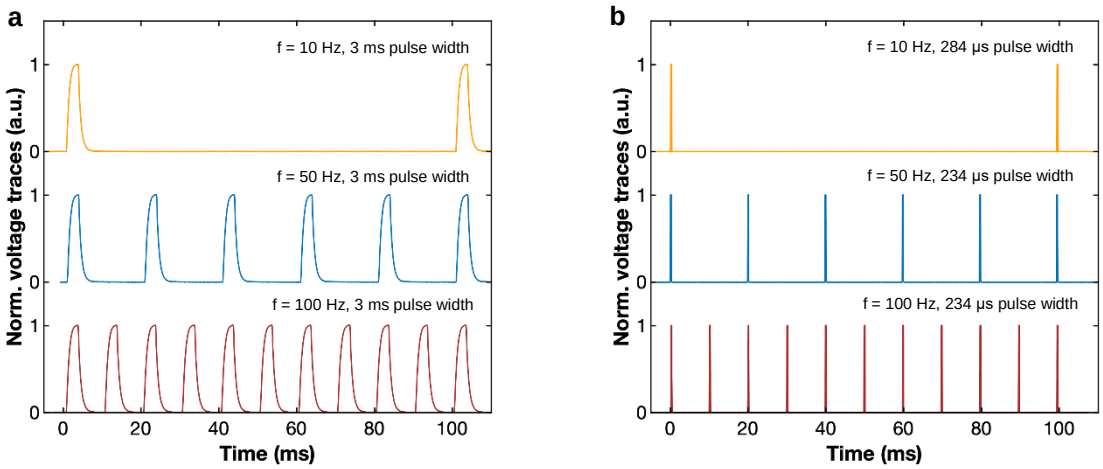

Figure S10. Demonstration of pulse duration limits. a, The shortest pulse achievable in the system that includes intensity control is 3 ms. The minimum pulse width is limited by the time constant of the analog filter used in the pulse width modulation (PWM) to analog conversion. **b**, In the system without the intensity control module, the achievable pulse widths are as short as 234 µs.

Supplementary Figure 11 – Schematic and operation of the control system

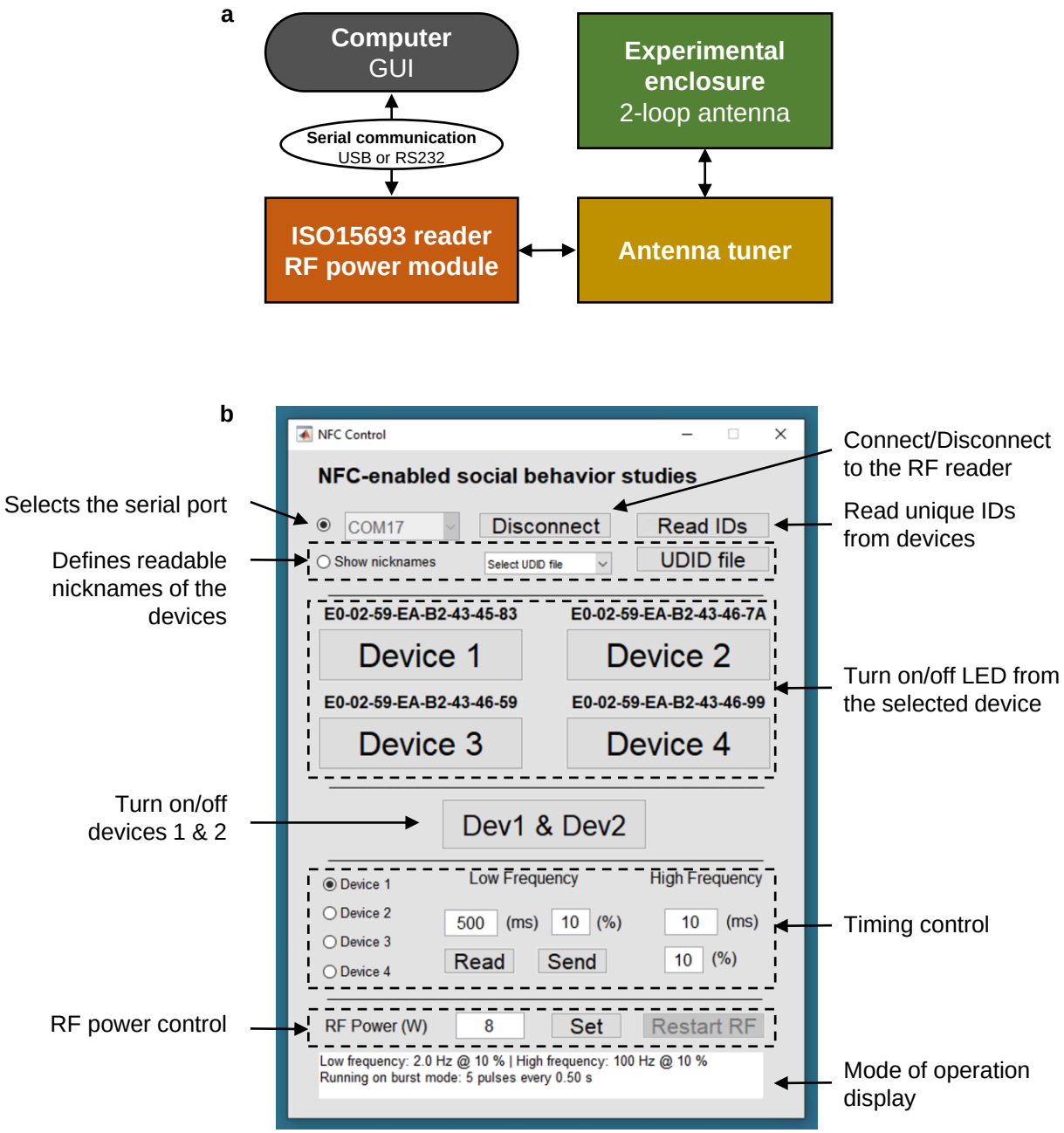

Figure S11. Schematic and operation of the control system. a, The control system is implemented in a custom-built MATLAB graphical user interface (GUI) that connects to a radio frequency (RF) power module and ISO15693 compliant reader via USB or serial RS232 interface. The GUI implements the corresponding NFC read/write commands addressed to the individual NFC chips contained in each active optogenetic device. The RF power module powers a dual loop antenna wrapped around the experimental enclosure and operating at 13.56 MHz. The antenna tuner provides impedance matching to resonantly transfer RF power and communication signals. Devices contained within the experimental enclosure can be individually addressed and controlled, as the basis for advanced behavioral studies. **b,** Graphical user interface implemented in MATLAB that enables the individual control of up to four devices in the experimental enclosure employed in the three-mice behavior paradigm studied in this work. The GUI also allows the modification of parameters such as the frequency, duty-cycle and RF power levels.

Supplementary Figure 12: LED characteristics

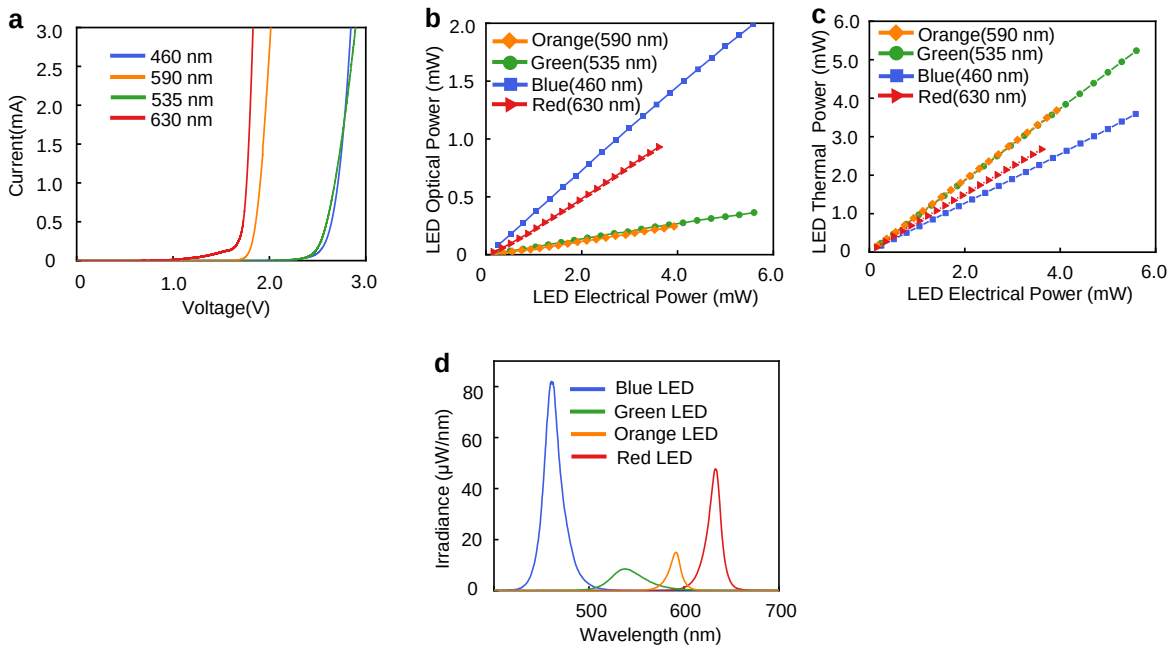

Figure S12. LED characteristics. a, μ-ILED IV curves (460 nm, 535 nm, 590 nm, 630 nm). **b,** μ-ILED optical power vs. μ-ILED electrical power for different wavelengths (460 nm, 535 nm, 590 nm, 630 nm). **c,** μ-ILED thermal dissipation vs. μ-ILED electrical power for different wavelengths (460 nm, 535 nm, 590 nm, 630 nm). **d,** μ-ILED emission spectra.

Supplementary Figure 13 – Optical emission profile of µ-ILED

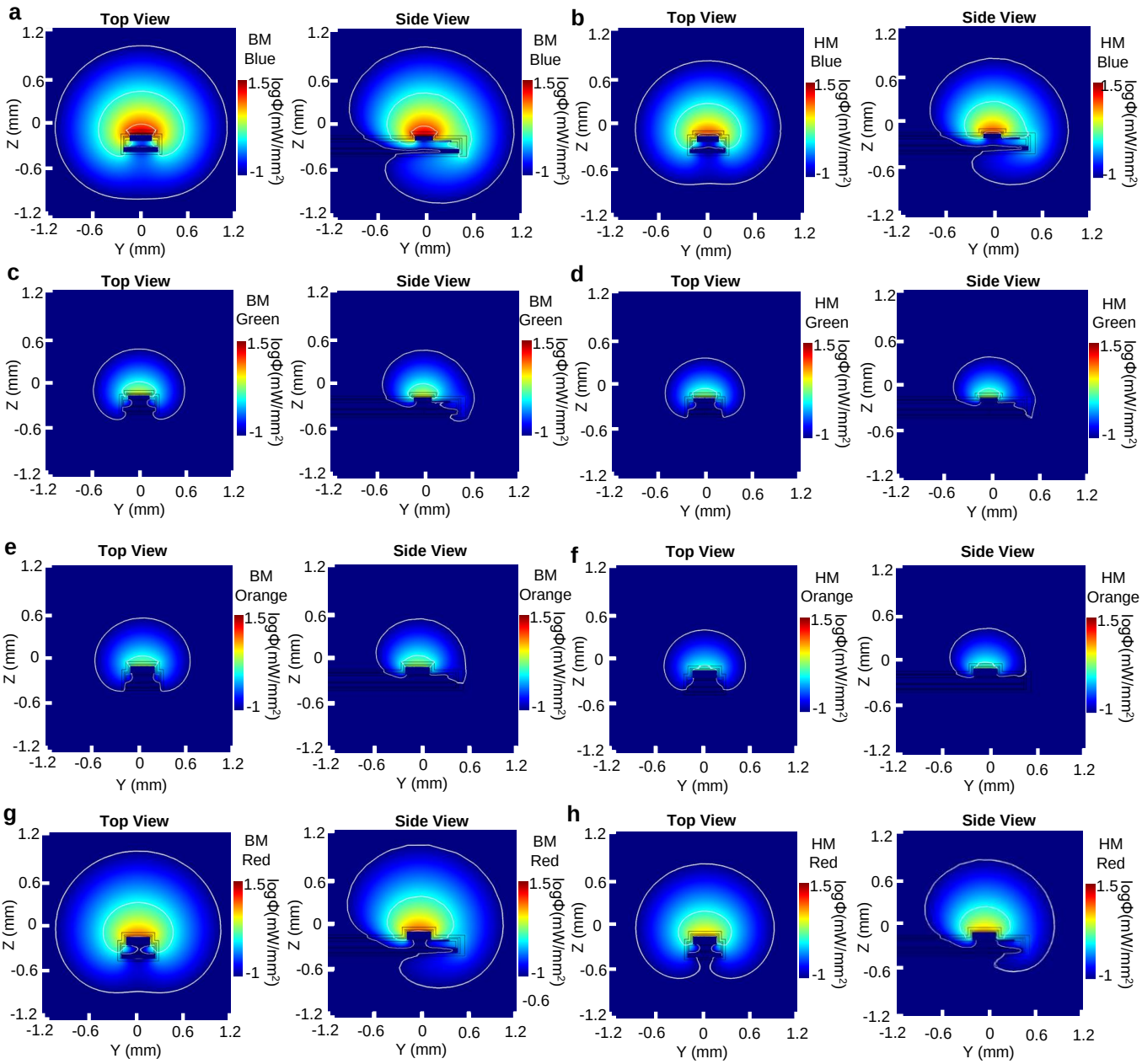

Figure S13. Optical emission profile of µ-ILED. a,b, Simulation of light penetration (460 nm) through brain tissue for back-mounted (BM) and head-mounted (HM) devices wirelessly powered with 8W of RF power applied to a transmission antenna. **c,d,** Simulation of light penetration (535 nm) through brain tissue for BM and HM devices wirelessly powered with 5W (to prevent overheating) and 8W of RF power applied to a transmission antenna. **e,f,** Simulation of light penetration (590 nm) through brain tissue for BM and HM device wirelessly powered with 6W and 8W of RF power applied to a transmission antenna. **g,h,** Simulation of light penetration (630 nm) through brain tissue for BM and HM device wirelessly powered with 8W of RF power applied to a transmission antenna.

Supplementary Figure 14 – Irradiance penetration profile associated with an µ-ILED operating in the brain

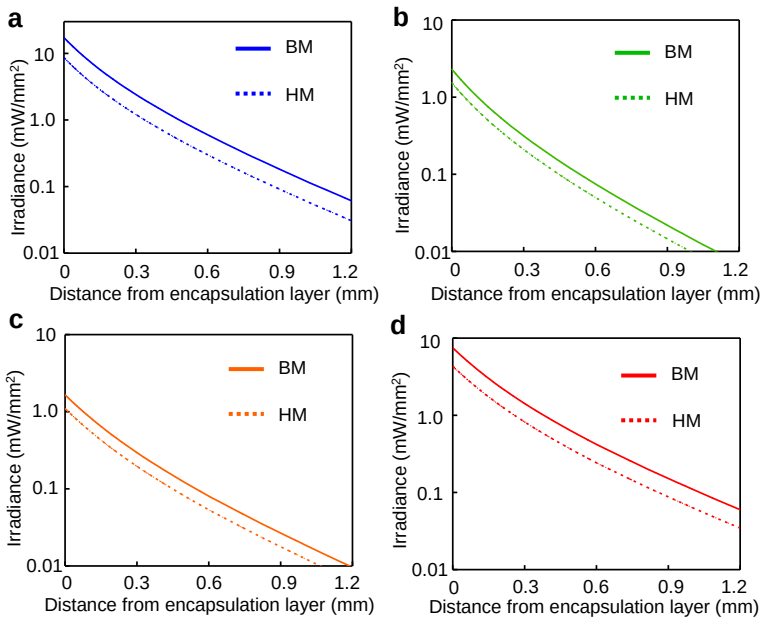

Figure S14. Irradiance penetration profile associated with an µ-ILED operating in the brain. a, Simulated irradiance as a function of penetration depth in brain tissue (460 nm). **b, c, d,** Same simulation as reported in (a) for different wavelengths at 535 nm, 590 nm, and 630 nm respectively.

Supplementary Figure 15 – Simulation results for changes in probe temperature during operation at 20 Hz and 40% duty cycle, for a BM device with different µ-ILEDs

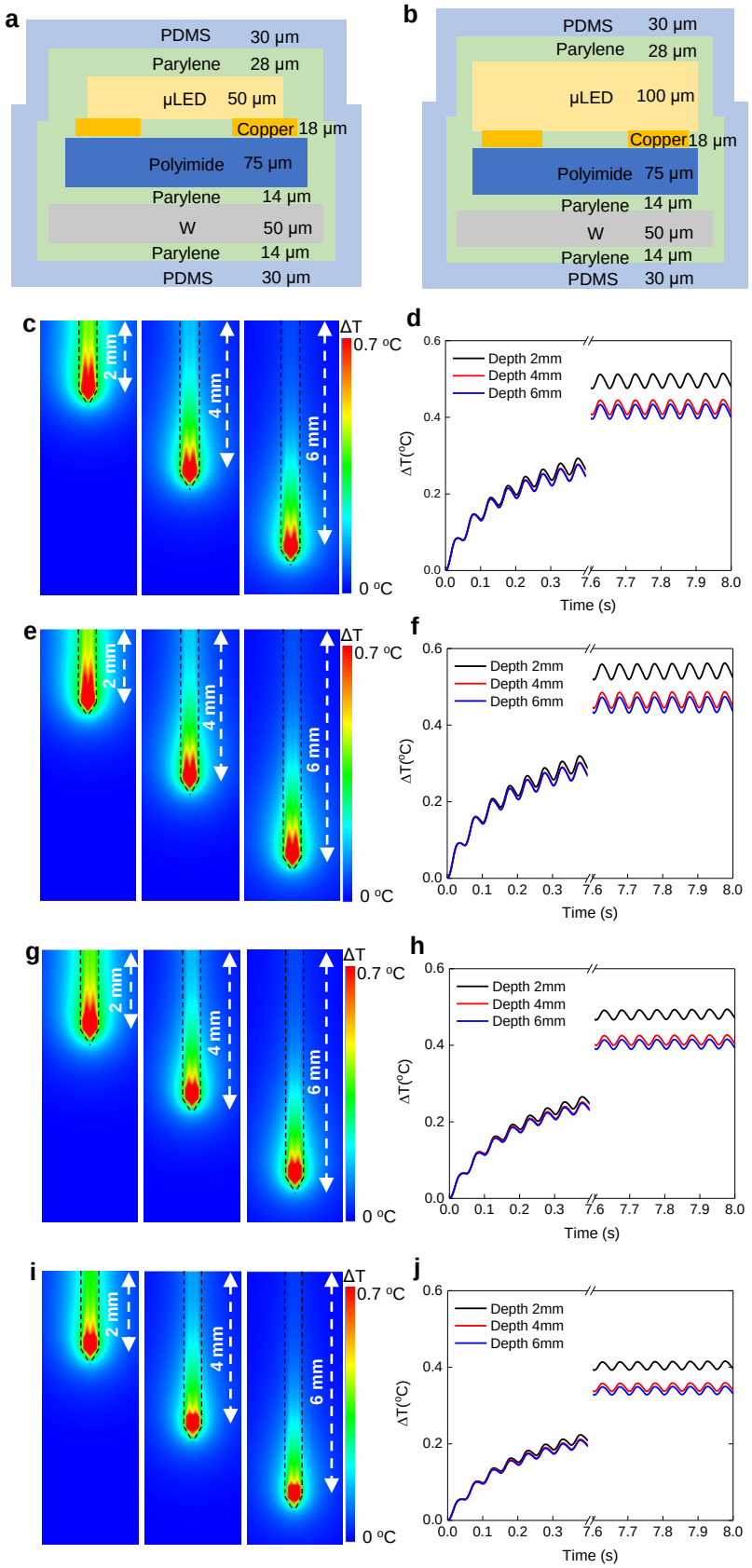

Figure S15. Simulation results for changes in probe temperature during operation at 20 Hz and 40% duty cycle, for a BM device with different µ-ILEDs. a, Cross sectional view of the encapsulation layout for probes with a blue (460 nm) or a green (535 nm) µ-ILED. **b,** Cross sectional view of the encapsulation layout for probes with an orange (590 nm) or a red (630 nm) µ-ILED. **c,** Simulated distribution of the change in temperature across the probe/tissue interfaces during operation (460 nm) at implantation depths of 2 mm, 4 mm, and 6 mm. **d,** Simulated distribution of the change in temperature at the probe tip (highest temperature) during operation (460 nm) as a function of time at implantation depths of 2 mm, 4 mm, and 6 mm. **e, f,** Same simulation as reported in (c) and (d) respectively for green (535 nm) µ-ILED. **g,h,** Same simulation as reported in (c) and (d) respectively for orange (590 nm) µ-ILED. **i,j,** Same simulation as reported in (c) and (d) respectively for red (630 nm) µ-ILED.

Supplementary Table S1 – Optical & thermal power output for HM and BM devices

a. Blue μ-ILED (460 nm)

	Transmission Antenna Power (W)	Optical Power (mW)	Thermal Power (mW)
HM	8	0.965	1.71
BM	8	1.93	3.41

b. Green μ-ILED (535 nm)

	Transmission Antenna Power (W)	Optical Power (mW)	Thermal Power (mW)
HM	8	0.170	2.40
BM	5	0.254	3.60

c. Orange μ-ILED (590 nm)

	Transmission Antenna Power (W)	Optical Power (mW)	Thermal Power (mW)
HM	8	0.155	2.27
BM	6	0.233	3.41

d. Red μ-ILED (630 nm)

	Transmission Antenna Power (W)	Optical Power (mW)	Thermal Power (mW)
HM	8	0.606	1.66
BM	8	1.05	2.88

a, Blue μ-ILED (460 nm). **b,** Green μ-ILED (535 nm), transmission antenna power at 5 W for BM scenario to prevent overheating. **c,** Orange μ-ILED (590 nm), transmission antenna power at 6 W for BM scenario to prevent overheating. **d,** Red μ-ILED (630 nm).

Supplementary Table S2 – Materials/tissue absorption coefficients μ_a (cm^{-1}) used in the optical and thermal simulations for different light wavelengths.

	Blue light (460 nm)	Green light (535 nm)	Orange light (590 nm)	Ref light (630 nm)
Fresh Brain [1]	4.47	5.90	4.90	4.30
Copper [2]	6.65×10^5	6.09×10^5	6.00×10^5	6.72×10^5
Tungsten [3]	5.47×10^5	5.47×10^5	5.47×10^5	5.47×10^5
Polyimide (PI) [4]	0.879	0.879	0.879	0.879
PDMS [5]	0.153	0.153	0.153	0.153
Parylene [6]	1.62	1.62	1.62	1.62
μ-ILED [7]	1.88×10^5	7.73×10^4	5.12×10^4	4.01×10^4

Supplementary Table S3 – Materials/tissue reduced scattering coefficients μ_s' (cm^{-1}) used in the optical simulations for different light wavelengths

	Blue light (460 nm)	Green light (535 nm)	Orange light (590 nm)	Ref light (630 nm)
Fresh Brain [1]	50.5	40.8	36.1	31.6
Copper	0	0	0	0
Tungsten	0	0	0	0
Polyimide (PI)	0.01	0.01	0.01	0.01
PDMS	0.001	0.001	0.001	0.001
Parylene	0.001	0.001	0.001	0.001
μ-ILED	0	0	0	0

Supplementary Table S4 – Materials/tissue thermal properties used in the heat-transfer simulation

	Thermal Conductivity k ($W \cdot m^{-1} \cdot K^{-1}$)	Specific Heat Capacity C_p ($J \cdot kg^{-1} \cdot K^{-1}$)	Density ρ ($kg \cdot m^{-3}$)
Fresh Brain	0.5	3700	1050
Copper	377	385	8960
Tungsten	163	134	1930
Polyimide (PI)	0.21	2100	909
PDMS	0.15	1460	970
Parylene	0.084	712	1289
μ-ILED	130	490	6100

Supplementary Table S5 – Summary of the bio-heat parameters [8] used in the thermal simulation

Variable	Parameter	Value	Units
ρ_b	Density of Blood	1060	$kg \cdot m^{-3}$
C_b	Specific Heat of Blood	3639	$J \cdot kg^{-1} \cdot K^{-1}$
ω_b	Blood Perfusion Rate	0.0085	s^{-1}
Q_{met}	Metabolic Heat Production (Brain)	9700	$W \cdot m^{-3}$
T_b	Arterial (core body) Temperature	309.85	K
T_o	Initial Brain Temperature	310.15	K

References

1. Mesradi, M. *et al.* Experimental and analytical comparative study of optical coefficient of fresh and frozen rat tissues. *J. Biomed. Opt.* **18**, 117010 (2013).
2. Johnson, P. B. & Christy, R. W. Optical Constants of the Noble Metals. *Phys. Rev. B* **6**, 4370–4379 (1972).
3. Ordal, M. A., Bell, R. J., Alexander, R. W., Newquist, L. A. & Querry, M. R. Optical properties of Al, Fe, Ti, Ta, W, and Mo at submillimeter wavelengths. *Appl. Opt.* **27**, 1203 (1988).
4. Zhang, Z. M., Lefever-Button, G. & Powell, F. R. Infrared Refractive Index and Extinction Coefficient of Polyimide Films. *Int. J. Thermophys.* **19**, 905–916 (1998).
5. Querry, M. Optical Constants of Minerals and Other Materials from the Millimeter to the Ultraviolet. 333 (1987).
6. Gatesman, A. J., Waldman, J., Ji, M., Musante, C. & Yngvesson, S. An Anti-Reflection Coating for Silicon Optics at Terahertz Frequencies. *IEEE Microw. Guid. Wave Lett.* **10**, 264–266 (2000).
7. Aspnes, D. E., Kelso, S. M., Logan, R. A. & Bhat, R. Optical properties of $Al_xGa_{1-x}As$. *J. Appl. Phys.* **60**, 754–767 (1986).
8. Stujenske, J. M., Spellman, T. & Gordon, J. A. Modeling the Spatiotemporal Dynamics of Light and Heat Propagation for In Vivo Optogenetics. *Cell Rep.* **12**, 525–534 (2015).